Tribology International 219 (2026) 111855

Contents lists available at ScienceDirect

Tribology International

journal homepage: www.elsevier.com/locate/triboint

Full length article

Experimentally validated numerical model for multi-physics simulation of friction, wear, and noise in dry sliding pin-on-disc configurations

Yang Tian, Muhammad Khan *

Centre of Life-Cycle Engineering and Management, Cranfield University, Bedford, Milton Keynes MK43 0AL, UK

ARTICLE INFO

Keywords:
Tribology
Friction
Wear
Frictional noise
Numerical modelling

ABSTRACT

Tribology plays a crucial role in engineering, where friction, wear, and noise in sliding contacts impact efficiency and durability. This study develops a novel numerical framework for simulating dry sliding wear in a pin-on-disc setup using 6082 aluminium discs and 304 stainless steel pins. The model integrates Zhang-Meng-Chen multi-regime contact mechanics, Hurtado-Kim scale-dependent adhesion friction, data-driven asperity interlocking correction, Archard-based wear evolution, and symbolic regression-derived noise prediction, initialized with statistically equivalent rough surfaces from profilometry data. Validated against experiments at 10–20 N loads and 0.42–0.84 m/s speeds, the framework accurately predicts coefficient of friction (COF) transitions from adhesion- to interlocking-dominated regimes, contact area evolution, asperity counts, wear volumes, and cumulative sound pressures, with mean relative errors below 16 %. Results reveal load-speed dependencies in friction mechanisms, surface topography changes, and acoustic emissions. This approach advances tribological modelling by linking microscopic interactions to macroscopic observables, paving the path for non-invasive machinery health monitoring through noise signals. Future enhancements could include thermal and debris effects.

1. Introduction

Tribology, the science of interacting surfaces in relative motion, plays a pivotal role in modern engineering by addressing friction, wear, and lubrication phenomena that directly influence energy efficiency, component durability, and system performance across industries such as automotive, aerospace, and manufacturing [1,2]. Globally, friction and wear account for approximately 23 % of total energy consumption, with mechanical losses in sliding contacts contributing significantly to equipment failures and maintenance costs [3]. In particular, the pin-on-disc configuration serves as a fundamental testbed for studying dry sliding wear, where dissimilar materials like aluminium alloys and stainless steel are commonly employed due to their widespread use in lightweight structures and corrosion-resistant applications [4–6]. However, predicting the tribological behaviour of such systems remains challenging owing to the multi-scale nature of surface interactions: at the microscopic level, asperity contacts govern elastic-plastic deformation, adhesion, and interlocking, while macroscopic outcomes manifest as evolving COF, wear volumes, and acoustic emissions arising from surface evolution and energy dissipation [7–9].

Recently, some studies have started to focus on the correlation between wear, COF, and noise during the sliding process. The experimental study measured the dependence of friction noise on the nominal contact area for rough surfaces under low normal load and constant sliding velocity, with the contact area varying over two orders of magnitude [10]. It identifies two regimes: one where vibration energy (and thus noise) is proportional to the contact area, and another where the energy remains constant, independent of the contact area, influenced by factors like internal damping. The study [11] investigated the roughness noise generated by friction between dry rough flat surfaces under light loads, attributing it primarily to impacts between antagonist asperities and demonstrating that it occurs even in dry conditions without significant influence from dynamic coupling or additional rigidity. The results reveal that the sound pressure level follows a logarithmic increase with both surface roughness and sliding speed. Abdelounis et al. [12] used a 2D explicit dynamic finite element model in ABAQUS software to simulate friction noise radiated from sliding contact between two rough dry surfaces under light load, incorporating real Gaussian surface topographies measured by profilometer and Coulomb's friction law at the interface. The simulations reveal that shocks

* Corresponding author.
E-mail addresses: muhammad.a.khan@cranfield.ac.uk, alikam85@gmail.com (M. Khan).

https://doi.org/10.1016/j.triboint.2026.111855
Received 20 October 2025; Received in revised form 3 February 2026; Accepted 15 February 2026
Available online 16 February 2026
0301-679X/Crown Copyright © 2026 Published by Elsevier Ltd. This is an open access article under the CC BY license (http://creativecommons.org/licenses/by/4.0/).

between antagonist asperities transfer kinetic energy to vibratory energy, leading to noise radiation, with the vibratory level increasing logarithmically with surface roughness and sliding speed, in agreement with experimental results and prior studies.

However, all aforementioned studies have not considered the wear-induced surface topology evolution, which influences the contact behaviour and noise. Although the upcoming studies [13,14] conducted by Lontin et al. incorporated the wear effect, however the model over-simplifies the contact between two rough surfaces into a rigid pin sliding over the beams in 2 dimensional, which deviates from the reality. The similar flaw can be found in studies [15,16], which simply attributes the friction noise to the vibration of the pin, without considering disc's contribution to the noise. Additionally, the study utilized the deep neuron networking (DNN) to predict the worn surface morphology and real time COF by noise signal [17]. Using the experimentally validated FEM wear model (because the real-time wear depth distribution variation is different to be experimentally measured), experimental COF, and noise as training dataset for DNN. Consequently, Tian et al. [18] developed a symbolic regression model quantitively bridging the noise, wear volume, and COF via the measured experimental data from ball-on-disc frictional pairs. Then, the mode was further validated on 3D-printed PLA materials sliding against the metal disc, aligning with experimental observations [19]. Although the model shows quite good prediction in noise, integrating this noise predicting model into a comprehensive numerical framework that bridges realistic surface generation, iterative topography updates, COF fluctuations remain elusive.

This study addresses this research gap by developing a novel numerical model that synergistically combines the ZMC multi-regime contact mechanics, HK scale-dependent adhesion friction, a data-driven asperity interlocking correction, Archard-based surface wear evolution, and a symbolic regression-derived noise prediction module. The model simulates the dynamic surface topography changes in a pin-on-disc setup, using statistically equivalent rough surfaces initialized from experimental profilometry data. Validated against pin-on-disc experiments conducted under dry sliding conditions at loads of 10–20 N and speeds of 0.42–0.84 m/s, the framework elucidates the transition from adhesion-dominated to interlocking-dominated friction, quantifies contact area and asperity evolution, and forecasts wear volumes and cumulative sound pressures with mean relative errors below 16 %. By distinguishing between adhesive and mechanical friction contributions while incorporating real-time surface topography updates, this approach advances tribological modelling toward more accurate predictions. It provides valuable insights into correlating noise signals with wear depth COF, thereby enabling non-intrusive monitoring of machinery health.

2. Methodology

2.1. Properties of specimens

The discs, having a diameter of 50 mm, were fabricated from 6082 aluminium alloy, while the pin, having a diameter of 4 mm, was fabricated from 304 stainless steel. The material properties of the discs and the pin are presented in Table 1 and Table 2, respectively. The Burgers vector (b) of 6082 aluminum is derived from its fcc lattice structure, using $b = a/\sqrt{2}$for the $1/2\langle 110\rangle$dislocation, where a is the lattice parameter of aluminum ($a \approx 0.405$ nm). Substituting yields $b \approx 0.286$ nm, consistent with experimental observations for Face-Centered Cubic Al-based alloys. Reported values of $b = 0.286$ nm are widely cited for pure and alloyed aluminum matrices [20–22].

Table 1
Mechanical Properties of Disc [18,20,21].

Symbol	Property	Value	Unit
ρ_1	Density	2700	kg/m^3
v_1	Poisson's Ratio	0.33	1
E_1	Young's Modulus	7.2E+ 10	Pa
G_1	Shear Modulus	2.6E+ 10	Pa
σ_{ys1}	Initial Yield Stress	2.71E+ 08	Pa
H	Hardness	125	Hv
b	Burgers Vector Length	2.86E-10	m

Table 2
Mechanical Properties of Pin [18].

Symbol	Property	Value	Unit
ρ_2	Density	8000	kg/m^3
v_2	Poisson's Ratio	0.3	1
E_2	Young's Modulus	2E+ 11	Pa
G_2	Shear Modulus	7.5E+ 10	Pa

2.2. Surface characteristics

The surfaces of both the pins and discs were measured using a profilometer. Subsequently, the measurement results were analyzed to obtain the height distribution, roughness, and asperity radius of the surfaces, as illustrated in Fig. 1 and Fig. 2. These surface roughness analysis results present a comparison between the disc and pin components, each measured three times to assess their surface characteristics. The disc exhibits higher surface roughness with *Ra* values ranging from 0.546 to 0.627 μm and sharp surface features indicated by small peak radii (0.019–0.038 mm), while the pin demonstrates a smoother surface profile with lower *Ra* values ranging from 0.337 to 0.359 μm and more rounded peaks as evidenced by larger peak radii (0.0059–0.019 mm).

Asperity peaks are identified using the multi-point 3-point peak (3PP) criterion, which was proposed by Pogačnik et al. [23]. The 3PP method identifies an asperity peak as any point on a surface profile (2D line profile) that is higher than both of its immediate neighboring points and lies above the profile mean line, with the asperity radius calculated as the radius of the circumcircle passing through the peak point and its two closest neighbors. The advantage of the 3PP criterion over the 5PP and 7PP criteria is that it provides more reliable and physically realistic results, since the number of asperity peaks decreases with increasing surface roughness (as expected from theoretical and experimental observations), whereas the 5PP and 7PP criteria yield nearly constant numbers of asperity peaks across varying roughness levels, which lacks physical justification.

The statistical distribution analysis reveals notable differences in surface topography: the disc shows negative skewness values (-0.104 to −0.215) indicating a predominance of valleys over peaks, with kurtosis values ranging from 2.570 to 3.043 suggesting near-normal to slightly peaked distributions, while the pin exhibits more negative skewness (-0.341 to −0.503) showing even more pronounced valley dominance and higher kurtosis values (3.725–4.575) indicating more peaked distributions with sharper height concentration. Both components display excellent statistical distribution fits (R^2 values ranging from 0.924 to 0.976).

The micromorphology and elemental distribution of the samples were analysed using a VEGA3 TESCAN, aiding in the identification of the wear mechanism.

2.3. Experimental design

Wear tests were conducted using the setup illustrated in Fig. 3 to evaluate friction, wear, and acoustic behavior in a pin-on-disc configuration. The apparatus (Fig. 3a) consists of a tribometer where a vertical 304 stainless-steel pin (Ø 4 mm, height 3 mm) is pressed against a rotating 6082 aluminium disc (Ø 50 mm, friction radius 20 mm) under controlled dry-sliding conditions. A microphone was positioned near the contact zone (0.1 m from the contact zone) to capture acoustic emissions during operation. Normal load (10–20 N) and sliding speed

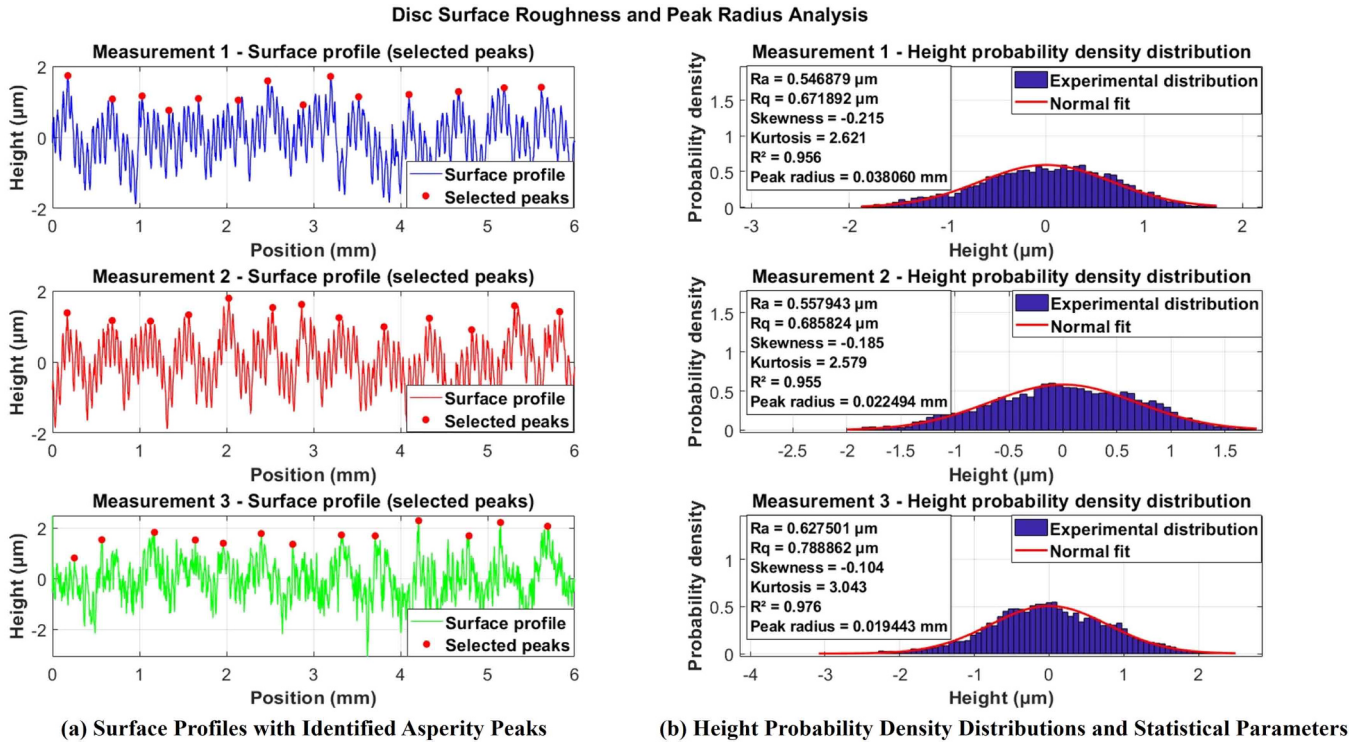


Fig. 1. Disc surface roughness and peak radius analysis (profile-based outputs), (a) Surface profiles with identified asperity peaks, (b) Height probability density distributions with normal fits and corresponding roughness parameters (R_a, R_q, skewness, kurtosis, and peak radius).

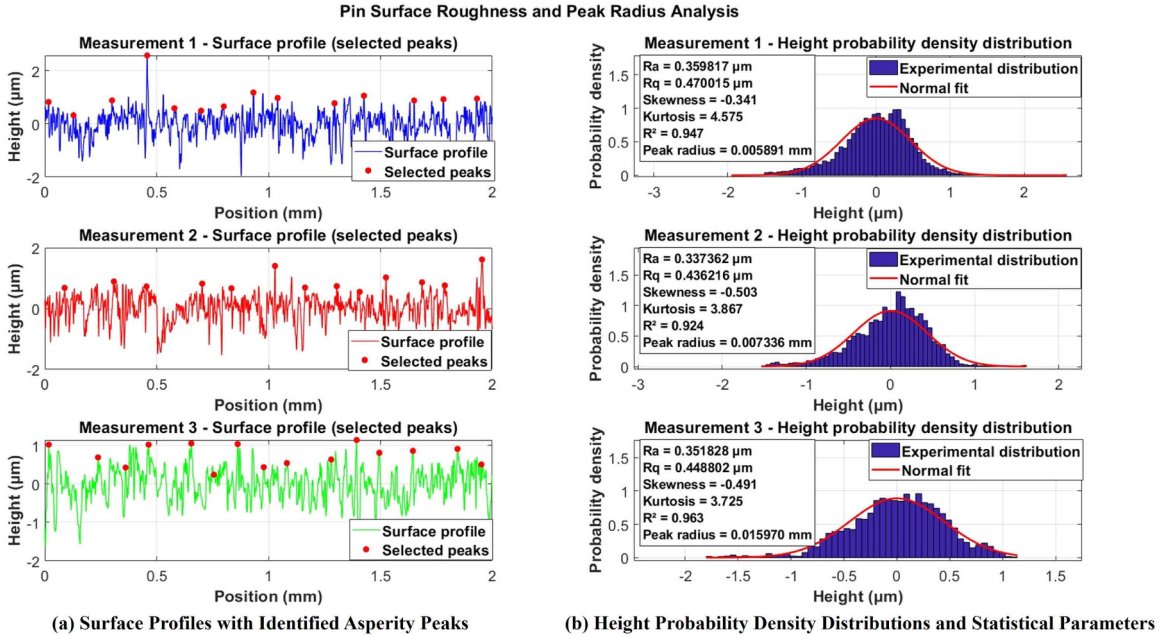


Fig. 2. Pin surface roughness and peak radius analysis (profile-based outputs), (a) Surface profiles with identified asperity peaks, (b) Height probability density distributions with normal fits and corresponding roughness parameters (R_a, R_q, skewness, kurtosis, and peak radius).

(0.42–0.84 m/s) were varied in a two-factor experimental matrix, while all other parameters were held constant to isolate the effects of load and speed. The normal force was applied through a calibrated pin holder to ensure uniform loading, creating representative sliding wear conditions that emulate real mechanical interfaces.

Prior to testing, both pin and disc surfaces were characterized by stylus profilometry (three repetitions per specimen) to determine arithmetic mean roughness, skewness, kurtosis, and asperity radius. These parameters were subsequently used to initialize the numerical rough-surface generator in the simulation. Each test lasted 60 s, during which tangential and normal forces, as well as acoustic pressure signals, were continuously recorded. After testing, the wear track depth was measured by profilometry (Fig. 3c), and the wear volume was calculated from the measured mass loss using the Archard model.

Each load-speed condition was repeated five times to ensure repeatability. One dataset per condition was used to fit the propor-

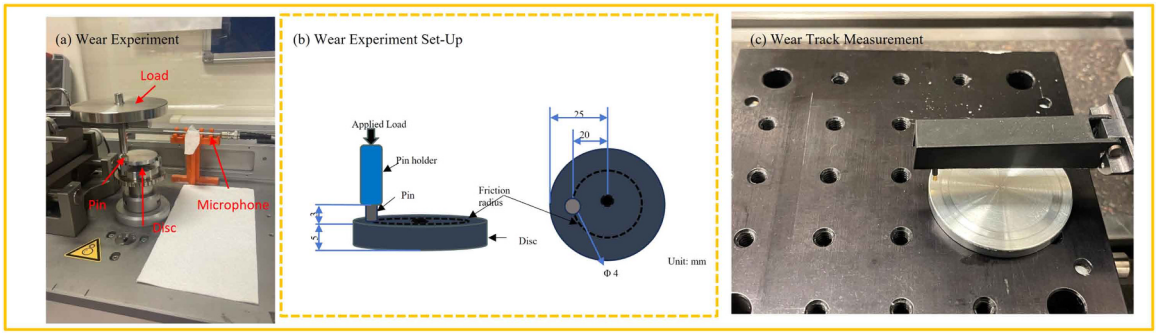


Fig. 3. Wear experiment and measurement procedure, Wear experiment and measurement procedure, (b) Schematic of the wear test configuration showing geometric dimensions and loading arrangement, (c) Post-test wear track measurement using a profilometer.

tionality constant A in the symbolic-regression noise model, while the remaining four were reserved for blind validation. Post-test optical microscopy and EDS analyses of the worn pins and discs confirmed the dominant wear mechanisms and verified the physical basis of the simulation assumptions.

2.4. Numerical model

This study implements a sophisticated surface wear simulation that combines multiple physics-based models to predict how rough surfaces evolve under sliding contact. The model integrates contact mechanics, friction analysis and prediction, and noise in a unified framework.

1. Surface Generation and Initialization

Directly analysing the contact between two rough surfaces is rather difficult. Therefore, the contact between the two rough surfaces is converted into a contact between a rigid flat surface and a statistical rough surface is a prevalent approach in contact mechanics due to its ability to simplify complex interactions and facilitate the analysis of contact parameters, see Fig. 4 [25–27]. The statistical surface generation module offers an advanced method for producing authentic rough surface topographies, with statistical parameters meticulously regulated according to the equivalent surface characteristics of the pin and disc, as outlined in Table 3. The process begins by establishing a circular specimen geometry (4 mm diameter), the contact area between the pin and disc, discretized into a high-resolution 1500 × 1500 grid, providing approximately 2.67 μm spacing between points to capture fine surface features, based on the number of asperities per unit length. The core generation starts with a base Gaussian random field created using MATLAB's randn function, which provides normally distributed height variations across the surface. However, real engineering surfaces rarely exhibit perfect Gaussian statistics, so the model employs an iterative statistical adjustment algorithm called that transforms this base surface to match target surface parameters: an arithmetic mean roughness (Ra_{eq}) of 0.675 μm, a negative skewness (Sk_{eq}) of −0.248, and a kurtosis (Ku_{eq}) of 3.050. The resulting surface serves as the initial condition for the wear simulation, providing a realistic starting topography that captures the complex height distributions found in actual engineering surfaces while maintaining mathematical control over the key statistical parameters that influence contact mechanics and tribological behaviour.

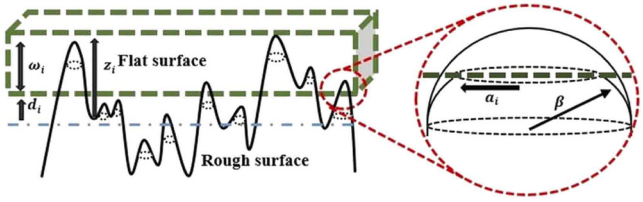


Fig. 4. Diagram illustrating a plane contacting an asperity featuring a spherical tip of radius abstracted from [24].

Table 3
Equivalent surface parameters of pin and disc to generate the initial rough surface.

Symbol	Property	Value	Unit
Ra_{eq}	Equivalent Arithmetic Mean Roughness	0.675	μm
Sk_{eq}	Equivalent Skewness	-0.248	1
Ku_{eq}	Equivalent Kurtosis	3.050	1
R_{eq}	Equivalent Asperity Radius	0.0071	mm

$$\begin{aligned} Ra_{eq} &= \sqrt{\left(Ra_{disc}^2 + Ra_{pin}^2\right)} \\ Sk_{eq} &= w_{d1} \times Sk_d + w_{p1} \times Sk_p \\ Ku_{eq} &= w_{d1} \times Ku_d + w_{p1} \times Ku_p \ \# \\ R_{eq} &= \frac{1}{\frac{1}{R_d} + \frac{1}{R_p}} \end{aligned} \tag{1}$$

Where Ra_{eq} is the equivalent arithmetic mean roughness, Ra_{disc} is the disc arithmetic mean roughness of three measurements (0.577441 μm), Ra_{pin} is the pin arithmetic mean roughness of three measurements (0.349668 μm). Sk_{eq} is the equivalent skewness, Sk_d (-0.168) and Sk_p (-0.445) are the skewness of disc and pin averaged over three measurements respectively. w_{d1} (73.2 %) and w_{p1} (26.8 %) are average weight parameters based on Ra_{disc} and Ra_{pin}. The weighting factors w_{d1} and w_{p1} quantify the relative contribution of the disc and pin roughness to the combined interface statistics. They were calculated from the squared roughness amplitudes, $w_{d1} = Ra_{disc}^2/(Ra_{disc}^2 + Ra_{pin}^2)$and $w_{p1} = Ra_{pin}^2/(Ra_{disc}^2 + Ra_{pin}^2)$, so that the rougher surface contributes more strongly to $Sk_{eq}$and Ku_{eq}. Ku_{eq} is equivalent kurtosis, Ku_d (2.749667) and Ku_p (3.789333) are the kurtosis of disc and pin averaged over three measurements, respectively. R_{eq} is the equivalent asperity radius, R_d is the average asperity radius of disc (0.026666 mm), R_p is the average asperity radius of pin (0.009732 mm).

2. Multi-Regime Contact Mechanics

Once the interference ω in Fig. 4 between a rough deformable surface and a rigid flat surface is determined, the deformations of each asperity in contact can be identified as elastic, elastoplastic, or plastic deformation. However, traditional contact models have focused on elastic [28,29] or plastic [30] deformations of asperities separately. Therefore, this study employs the Zhang-Meng-Chen (ZMC) model [31] to capture the complex transition from elastic to fully plastic deformation that occurs when surface asperities come into contact under load. This sophisticated approach recognizes that real surface contacts do not simply jump from elastic Hertzian

behaviour to fully plastic flow but instead undergo a gradual transition through an elastoplastic regime where both elastic and plastic deformation mechanisms are active simultaneously. The model defines three distinct contact regimes based on the dimensionless relative deformation parameter ω/R (Eq. (2)), where R is the asperity radius. By employing the condition that the total normal forces from the asperities balance the applied force, an iterative approach is applied to calculate the interference depth between the flat and rough surfaces that satisfies this criterion.

$$\begin{aligned} F_e &= \frac{4}{3}E_{eq}R^{\frac{1}{2}}\omega^{\frac{3}{2}}, \quad \omega \Big/ R \le \omega_1 \quad ,\text{Elastic Contact} \\ F_{ep} &= \left[H - H(1-k_f)\frac{\ln\omega_2 - \ln\omega}{\ln\omega_2 - \ln\omega_1}\right]A_{ep}, \quad \omega_1 < \omega \Big/ R < \omega_2, \text{Elatoplastic Contact\#} \\ F_p &= 2\pi R\omega H, \quad \omega_2 < \omega/R, \text{Plastic Contact} \end{aligned} \tag{2}$$

In the first regime ($\omega/R \le \omega_1$), the pure elastic contact follows classical Hertzian theory, where E_{eq} is the equivalent elastic modulus calculated from both materials' properties, $1/E_{eq} = (1 - \nu_1)/E_1 + (1 - \nu_2)/E_2$. The critical transition parameter $\omega_1 = (\frac{3\pi k_f H}{4E_{eq}})^2$ depends on the material hardness H, equivalent modulus E_{eq}, and the factor $k_f = 0.25$ [32].

In the intermediate elastoplastic regime ($\omega_1 < \omega/R < \omega_2$), a sophisticated interpolation is employed, where the contact area is modified by a cubic polynomial function $A_{ep} = \pi R\omega\left[1 - 2\left(\frac{\omega-\omega_1}{\omega_2-\omega_1}\right)^3 + 3\left(\frac{\omega-\omega_1}{\omega_2-\omega_1}\right)^2\right]$, while the contact pressure gradually increases from the elastic value to the material hardness H through a logarithmic relationship, with $\omega_2 = 54\omega_1$ [24].

Finally, in the fully plastic regime ($\omega_2 < \omega/R$), the contact pressure reaches the material hardness limit, and the contact force becomes $F_p = H{\cdot}A_p$ with the contact area $A_p = \pi R\omega$, representing complete plastic flow of the asperity.

3. Scale-Dependent Adhesion Friction

The LuGre friction model is one of the most widely used friction models, which models the friction interface as deformable bristles on one surface contacting a rigid surface, capturing hysteresis, spring-like stiction (static friction), frictional lag, varying break-away force, and stick-slip motion [33]. However, the parameters of the model are difficult to identify, which results in difficulties in employing the model. A subsequent study identifies the parameters by collecting tangential force and velocity data from dry friction experiments, defining an objective function as the RMS of the normalized error between model predictions and experimental hysteresis curves, and optimizing the parameters using an improved quantum genetic algorithm [34]. Since the parameters of the model are derived from the stable state of the tribological system, integrating the LuGre friction model into the modelling of surface evolution due to wear—a dynamic process—would not be feasible.

Therefore, the scale-dependent Hurtado-Kim (HK) friction model is implemented, which captures the experimentally observed phenomenon that friction stress varies significantly with contact size, departing from the classical assumption of a constant friction coefficient across all scales [35]. This sophisticated approach recognizes the scale-dependent sliding friction behaviour, with smaller contacts exhibiting higher friction stresses due to the increased influence of interfacial adhesion. This friction model can be integrated with models of the dynamic contact area evolution due to surface evolution caused by wear.

The model characterizes the contact of each asperity using a dimensionless size parameter $\alpha = a/b$, where a is the contact radius and $b = 2.86 \times 10^{-1}$ °m is the Burgers vector. The friction stress then follows a three-regime piecewise relationship, as shown in Fig. 5.

For small contacts ($\alpha < a_1 = 28$), the friction stress remains at a high constant value $\tau f_1 = 1/43$ of the effective shear modulus, representing atomic-scale adhesive friction where individual asperity contacts cannot accommodate significant plastic flow; for intermediate contacts ($a_1 \le \alpha < a_2 = 9 \times 10^4$), the friction stress decreases according to a power-law relationship $\tau f = 10^{\wedge}(Mf{\cdot}\log_{10}(a) + Bf)$, where the scaling parameters Mf and Bf are derived from the boundary conditions to ensure smooth transitions between regimes; and for large contacts ($\alpha \ge a_2$), the friction stress reaches a minimum value $\tau f_2 = 1/1290$ of the shear modulus, representing macroscopic sliding where extensive plastic accommodation reduces the effective friction stress.

The effective shear modulus $G_{eq} = \frac{2G_1G_2}{G_1+G_2}$ combines the shear moduli of aluminum (26 GPa) and steel (75 GPa) materials. Furthermore, the final adhesion friction force F_{ad} is the sum of the adhesion friction forces at each contact, calculated as the product of the size-dependent friction stress τf_i and the contact area A_i.

$$F_{ad} = \sum_i^n \tau f_i A_i \# \tag{3}$$

This scale-dependent approach provides a physically realistic representation of how friction evolves from atomic-scale adhesive interactions to macroscopic sliding mechanics, enabling the model to accurately predict friction behaviour across the wide range of contact sizes (from nanometres to micrometres) that simultaneously exist on real rough surfaces during sliding contact.

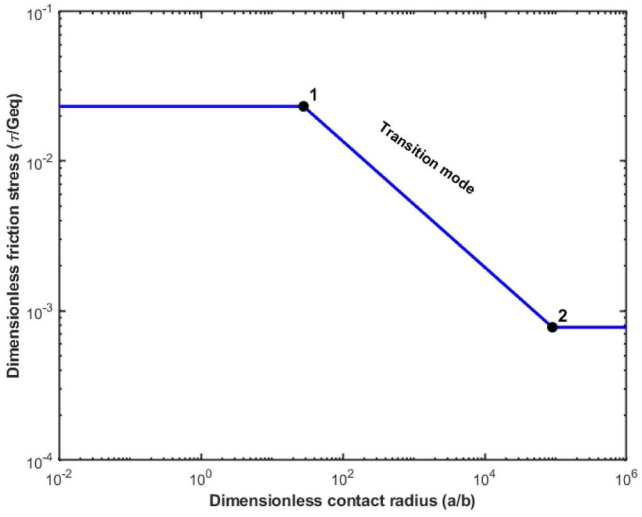


Fig. 5. Schematic of Dimensionless Friction Stress vs. Dimensionless Contact Radius(reproduced from [35,36]).

However, by simplifying the contact between two rough surfaces to a flat-rough surface interaction, the model neglects the interlocking of asperities that resists sliding motion and contributes to friction as well. So, to accurately capture the friction behaviour, the asperity interlocking induced friction needs to be considered.

4. Asperity Interlocking Friction

To the best of the authors' knowledge, no applicable physical model currently exists to quantify the friction induced by asperity interlocking. Since previous studies have primarily considered adhesion friction, leading to predicted COF values that are smaller than those observed experimentally. A feasible approach to quantify the interlocking friction involves calculating the difference between the experimental COF and the adhesion COF—namely the interlocking friction—and fitting a quantitative relationship among the total contact area A, the number of asperities in contact N, and the wear volume V, see Eq. (4). This is because asperity interlocking is governed by these three factors, which are dynamically updated at each simulation step according to the evolving surface morphology and instantaneous contact conditions.

$$F_{interlocking} = F_n \cdot (\text{-}8.777981 \ + \ \text{-}0.492058 \cdot 1\text{n}\ (\text{A}) \ - \ 0.115090 \cdot 1\text{n}\ (\text{N}) \ + \ 0.122017 \cdot 1\text{n}\ (\text{V}))\# \tag{4}$$

The asperity-interlocking friction term captures how evolving surface morphology affects mechanical interlocking:

- **Real contact area (A)**: Initially increases interlocking by enlarging asperity junctions, but excessive plastic conformity smooths the surface, thus reducing interlocking (negative coefficient).
- **Asperity count (N)**: A higher number of load-bearing asperities distributes the load more evenly and lowers local deformation, thereby decreasing interlocking friction (negative coefficient).
- **Wear volume (V)**: Progressive wear first roughens and enhances micro-interlocking but later polishes the surface, leading to a transient increase followed by reduction in interlocking friction (positive coefficient reflects this early growth).

Eq. (4) is a physics-guided semi-empirical equation for asperity-interlocking friction, constructed by attributing the residual friction $\mu_{\text{interlocking}} = \mu_{\text{total}} - \mu_{\text{adhesion}}$ to morphology descriptors (A, N, V) that evolve during sliding. Because interlocking depends on material pair, roughness statistics, third-body formation, lubrication state, and operating window, the fitted coefficients in Eq. (4) are specific to the tribosystem and parameter ranges studied here. The equation should therefore not be interpreted as a universal friction law; rather, its functional form may be reused for other systems, but coefficient recalibration is required when materials, surface preparation, environment, or wear regime changes.

So, the total friction force is the sum of two components, adhesion and interlocking.

$$F_f = F_{ad} + F_{interlocking}\# \tag{5}$$

5. Archard Wear Model Based Surface Evolution

In general, there are three of the most widely applied wear models: the Archard model, the continuum damage mechanics (CDM) model, and the Aghababaei wear model (AWM).

The Archard wear evolution component represents the core mechanism by which the surface topography dynamically changes throughout the simulation, implementing a localized, pressure-dependent wear model that continuously updates the three-dimensional surface geometry based on the contact mechanics at each asperity [37–39]. The implementation follows the classical Archard wear equation in its fundamental form:

$$H_w = \frac{K_{wear} \cdot P \cdot S}{H}\# \tag{6}$$

Where H_w is the wear depth, K_{wear} is the dimensionless wear coefficient for the aluminium–steel pair, determined by substituting the experimentally measured wear track depth into Archard's equation, P is the contact pressure calculated individually for each active asperity as the ratio of contact force to contact area, H is the hardness of softer material (aluminium), and S is the sliding distance calculated per time step.

The continuum damage mechanics (CDM)-based wear model aims to predict material wear by treating it as a progressive accumulation of damage, represented by a continuous scalar variable that evolves under stress, strain, and thermodynamic irreversibility until reaching a critical threshold that signifies material removal as wear particles [40,41].

In the AWM model, the critical junction size is a key concept in modern adhesive wear models that determines whether sliding contact between asperities on rough surfaces results in plastic deformation (no wear) or the detachment of a wear particle (wear). It arises from a Griffith-like energy balance criterion, comparing the elastic energy released during potential debris formation to the adhesive (or fracture) energy required to create new free surfaces [42–44].

However, due to instrumental limitations in our lab, some parameters required for the CDM and AWM models are not accessible to us through experimental measurement. Therefore, the Archard model was implemented to simulate the surface evolution.

6. Noise Prediction

Tian et al. [22] developed a symbolic regression-based model linking wear volume, cumulative noise pressure, and the COF, as shown in Eq. (7).

$$P_{\text{cumulative}} = A \cdot \sqrt{V_m} \cdot \mu \tag{7}$$

Where $P_{\text{cumulative}}$, referred to as cumulative sound pressure, is the total sound pressure level experienced over a period of time due to repeated or prolonged exposure to noise (unit: Pa). It is typically measured to assess the potential impact of noise on human health, hearing, or environmental conditions. V_m is wear volume (unit: m^3), μ is the COF, and A (unit:$kg \cdot m^{-4} \cdot s^{-2}$) is a constant derived by fitting data from various experimental conditions.

Fig. 6 illustrates the flowchart of the proposed methodology, detailing how friction analysis, wear prediction, and noise prediction are conducted through an iterative time-stepping approach. The simulation commences with input parameters, including normal load (Fn), sliding velocity (V), and initial surface characteristics (height Z_{i1}, equivalent roughness Ra_{eq}, skewness Sk_{eq}, and kurtosis Ku_{eq}), followed by a time loop in which three interconnected models operate sequentially. The ZMC contact model initially evaluates the contact mechanics between surface asperities, integrating a load-balancing condition ($Fn = Ft$) to ensure equilibrium and yielding interference values (ω_{ij}), contact radii

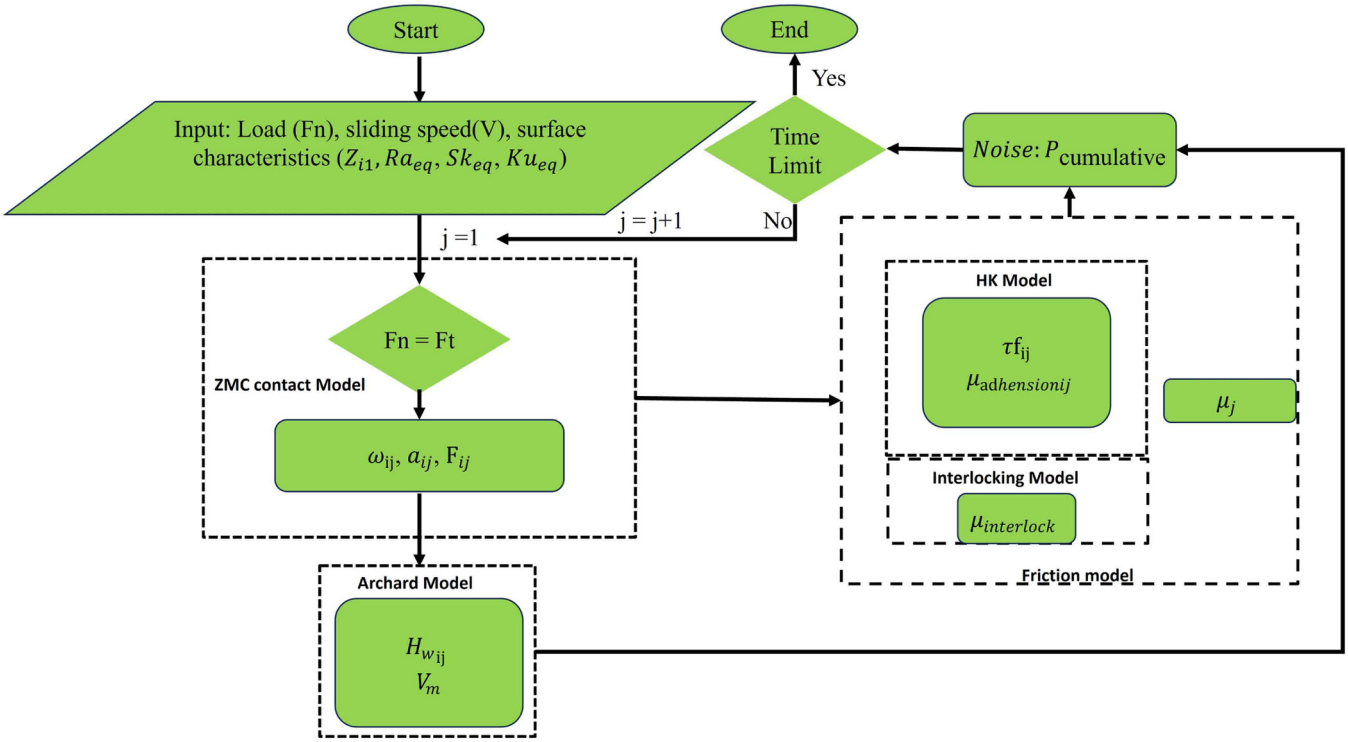


Fig. 6. Integrated Contact-Friction-Wear Simulation Framework.

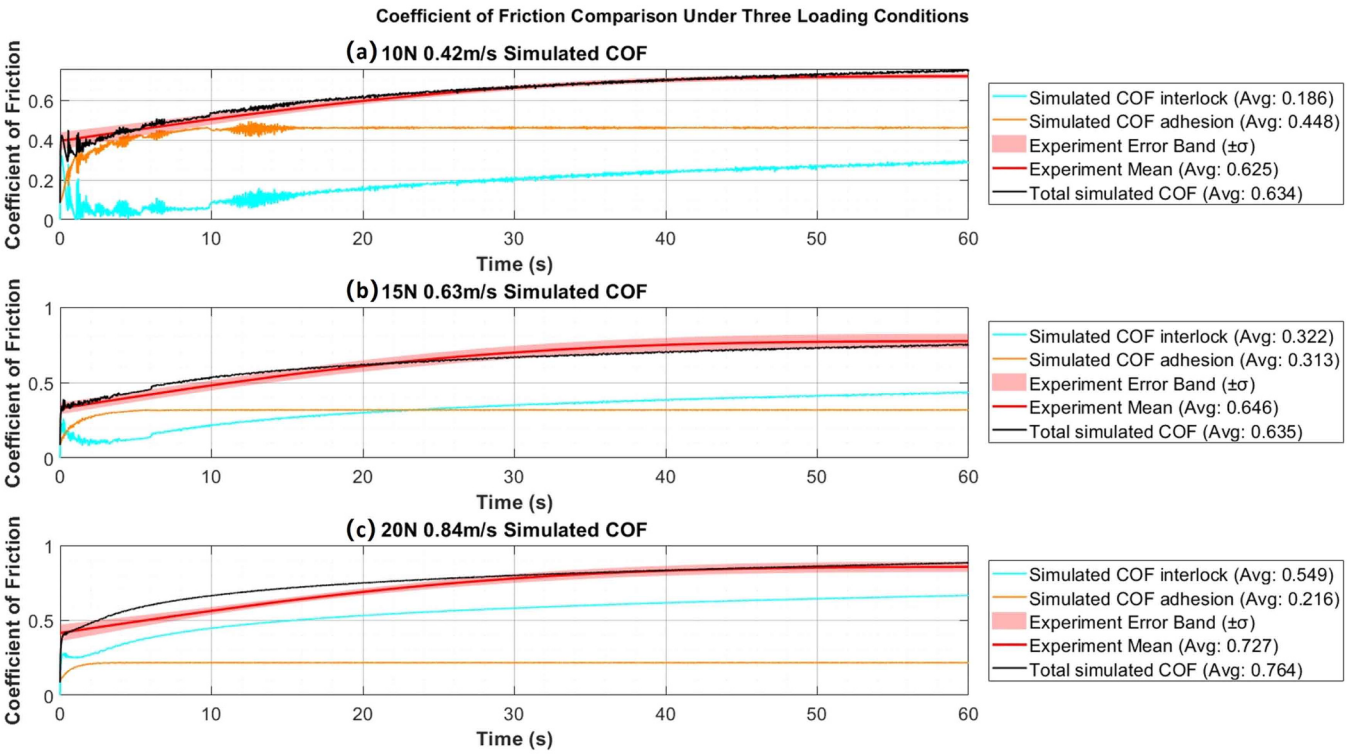


Fig. 7. COF comparison between experiment and simulation under different loading conditions, (a) 10 N, 0.42 m/s, (b) 15 N, 0.63 m/s, and (c) 20 N, 0.84 m/s.

(a_{ij}), and contact forces (F_{ij}) for each asperity contact. These results inform an innovative dual-component friction model that integrates the Hurtado-Kim (HK) model for scale-dependent adhesion friction (calculating τf_{ij} and $\mu_{adhensionij}$) with a novel interlocking model ($\mu_{interlock}$) to compute the total friction coefficient ($\mu_j = \mu_{adhensionij} + \mu_{interlock}$), constituting a pioneering approach that distinguishes between adhesive and mechanical geometric contributions to friction. The contact and friction outputs subsequently drive the Archard wear model, which predicts wear depth (H_{wij}) and volume (V_m) at each contact point as a function of local contact pressures. A pivotal feature of this model is its feedback mechanism, whereby wear-induced surface changes update

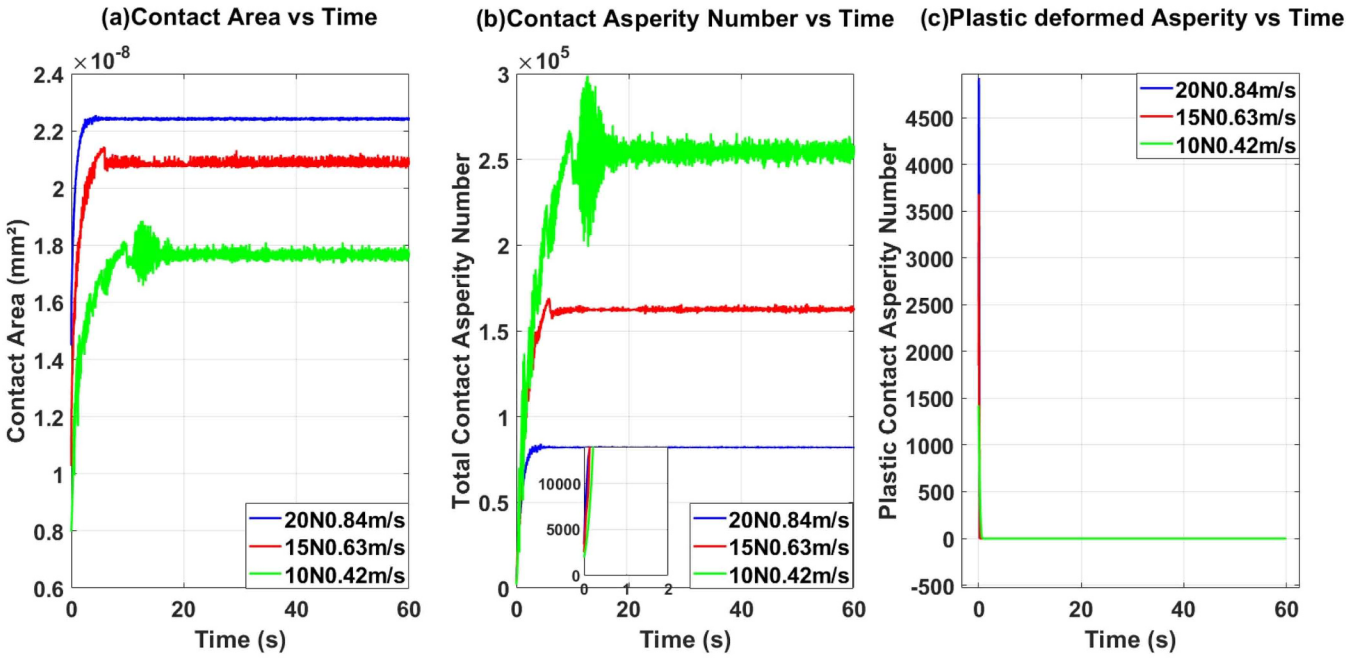


Fig. 8. Contact mechanics evolution under different loading conditions, (a) Contact area versus time, (b) total asperity number versus time, and (c) plastically deformed asperity number versus time for 10 N–0.42 m/s, 15 N–0.63 m/s, and 20 N–0.84 m/s.

the surface characteristics for subsequent time steps, facilitating a realistic evolution of surface topography over time, while a noise prediction component ($P_{\text{cumulative}}$) is calculated by the COF and wear evolution.

3. Results and discussion

3.1. Coefficient of friction

Fig. 7 presents COF under three different loading conditions: 10 N at 0.42 m/s, 15 N at 0.63 m/s, and 20 N at 0.84 m/s, respectively, showing simulated results aligning with experimental data over a 60-second timeframe. A consistent pattern emerges across all loading conditions: the COF starts low and gradually increases over time, eventually plateauing at values between 0.6 and 0.8. Notably, as the loading conditions increase in severity (higher force and speed), the final equilibrium COF values show a slight upward trend, indicating that more aggressive loading conditions result in higher steady-state friction coefficients.

Adhesion COF initially increases and eventually stables because of the contact area increases and then stables with the wear progress caused surface evolution [45,46], which can also be seen from the result of this study result Fig. 8. Interlocking COF initially presents high value due to strong asperity interlock in running-in phase, and decreases with the wear progress caused surface evolution, as the asperities are worn off, leading to a more uniform load distribution [47]. However, interlocking COF rise up at the late stage, especially under higher load and speed. Since, we attribute other factors affecting COF into interlocking effect, this phenomenon might be caused by the friction heat induced aluminium softening, so the steel pin penetrates into the aluminium disc deeper, therefore, COF is increased [48].

Under 10N0.42 m/s, the simulated interlocking COF consistently shows lower values compared to the adhesion component, which indicates the inter surface adhesion is the dominant resistance to prevent the relative sliding. Under 15N0.63 m/s, the simulated interlocking COF initially shows lower values compared to the adhesion component, then exceeds the adhesion COF around the 20 sec, which shows the change of the dominant friction mechanism. When the load and speed are further increased to 20 N and 0.84 m/s, interlocking COF consistently shows higher values in comparison with adhesion COF. Actually, through comparing the average values of adhesion and interlocking COFs under different loading conditions, we can see increase load and speed, leading to the enhance of interlocking COF but the decrease of adhesion COF. The higher load strengthens the interlocking effect between the asperities at the interface, but also increases the contact area on each asperities in contact, which turns the contact area from atomic scale to micro scale reducing adhesion COF [35,36].

3.2. Contact area and asperity in contact

Fig. 8 presents a comprehensive analysis of contact mechanics under three different loading conditions (20 N at 0.84 m/s, 15 N at 0.63 m/s, and 10 N at 0.42 m/s). Fig. 8(a) demonstrates contact area evolution over time, wherein all three conditions exhibit rapid initial growth within the first 5–10 s before stabilizing at distinct steady-state values: the highest load-velocity condition (20 N at 0.84 m/s) achieves the largest contact area of approximately 2.25×10^{-8} mm^2, followed by the intermediate condition (15 N at 0.63 m/s) at approximately 2.1×10^{-8} mm^2, and the lowest condition (10 N at 0.42 m/s) at approximately 1.8×10^{-8} mm^2. Higher normal loads generate greater contact pressure, which causes more surface asperities to deform and establish contact. This behaviour is consistent with classical contact mechanics theories, such as Hertzian contact theory, wherein contact area scales with load. The increased force physically pushes the surfaces together more firmly, thereby flattening more surface roughness and creating a larger real contact area.

Fig. 8(b) discloses the total contact asperity numbers over sliding process. Initially, an increased load leads to a greater number of asperities in contact; however, as wear progresses and surface morphology evolves, asperity counts stabilize at steady-state values, exhibiting a counterintuitive inverse relationship with the load and velocity increase: the lowest load condition sustains the highest asperity count ($\sim 2.5 \times 10^6$), the intermediate condition stabilizes at $\sim 1.7 \times 10^6$, and the highest load condition attains equilibrium at the lowest value ($\sim 0.8 \times 10^6$). In the stable phase, under higher load conditions, fewer asperities are in contact, yet the total contact area is larger, suggesting a greater average contact area per individual asperity.

Fig. 8(c) illustrates the number variation of plastic contact asperities, where only the highest load-velocity condition (20 N, 0.84 m/s) demonstrates substantial plastic deformation, with an initial spike of approximately 4500 plastic asperities before swiftly declining to near zero, while the two lower conditions exhibit minimal plastic contact throughout the entire 60-second observation period.

The number of plastically deformed asperities decreases to nearly zero after the initial running-in stage under all conditions. This trend is primarily a consequence of the contact idealization adopted in the model, where the interaction between two rough surfaces is transformed into an equivalent problem: a rigid flat surface in contact with an "equivalent" deformable rough surface obtained from the original two rough surfaces (a common simplification for rough–rough contact).

At the beginning of sliding, only a small population of the highest asperities makes contact with the rigid flat, which leads to locally high contact pressures and plastic deformation at these few load-bearing summits. As the wear process proceeds, these high asperities are rapidly removed. The remaining surface topography becomes progressively more conformal, and a larger number of asperities with comparable heights share the external load. Consequently, the load carried by each individual asperity decreases, reducing the local contact pressure and driving the predicted number of plastically deformed asperities toward zero in subsequent simulation steps.

However, that in real tribological contacts a non-zero fraction of asperities may continue to experience plastic deformation due to ongoing roughness regeneration, third-body effects, and local stress concentrations. Therefore, the current framework may be conservative (or may under-predict plasticity) for worn surfaces after running-in phase.

3.3. Worn trace and wear volume

Fig. 9 presents a comparative analysis of wear profiles under three different loading conditions: 10 N at 0.42 m/s, 15 N at 0.63 m/s, and 20 N at 0.84 m/s. Each subplot displays three profiles along the surface length: the simulated initial profile, the simulated worn profile, and the experimentally measured wear profile. With increasing applied load and sliding speed, the depth and width of the wear track also increase. Under 10 N at 0.42 m/s, the experimental profile exhibits a shallow wear depth (−15 μm), slightly deeper than the simulated wear (−10 μm). Under 15 N at 0.63 m/s, both simulation and experimental results indicate a deeper wear region, with the experimental profile reaching approximately −25 μm. Under 20 N at 0.84 m/s, significant wear is observed, with the experimental profile reaching approximately −45 μm, while the simulated profile underestimates the depth at approximately −40 μm.

Overall, the simulation captures the trend of increasing wear with load but consistently underestimates the maximum wear depth observed experimentally. This discrepancy can be attributed to the wear coefficient used in the simulation, typically derived from averaged experimental measurements. In certain regions, the simulated wear depth exceeds experimental measurements, whereas in others, it is lower than experimental measurements. Additionally, experimental setups often involve vibrations, misalignments, thermal effects, and contaminants (e.g., wear debris), which are not accounted for in the model and contribute to discrepancies between simulation and experimental results [49–51].

Fig. 10 presents the analysis of wear volume through simulated time series and experimental comparisons under three test conditions. The wear volume can be approximated from the measured wear track depth by first obtaining the cross-sectional area of the wear scar — by integrating the depth profile $A_c = \int h(x)dx$. This area is then multiplied by the track's circumference to give the total experimental wear volume, $V_w = 2\pi r_f A_c$. For each configuration, three repeats were used for K_{wear} calibration (the mean value was taken to reduce random test-to-test scatter), and the remaining two repeats were reserved as an independent validation set for Fig. 10 (reported as mean ± standard deviation). This ensures that the agreement in Fig. 10 demonstrates the model's

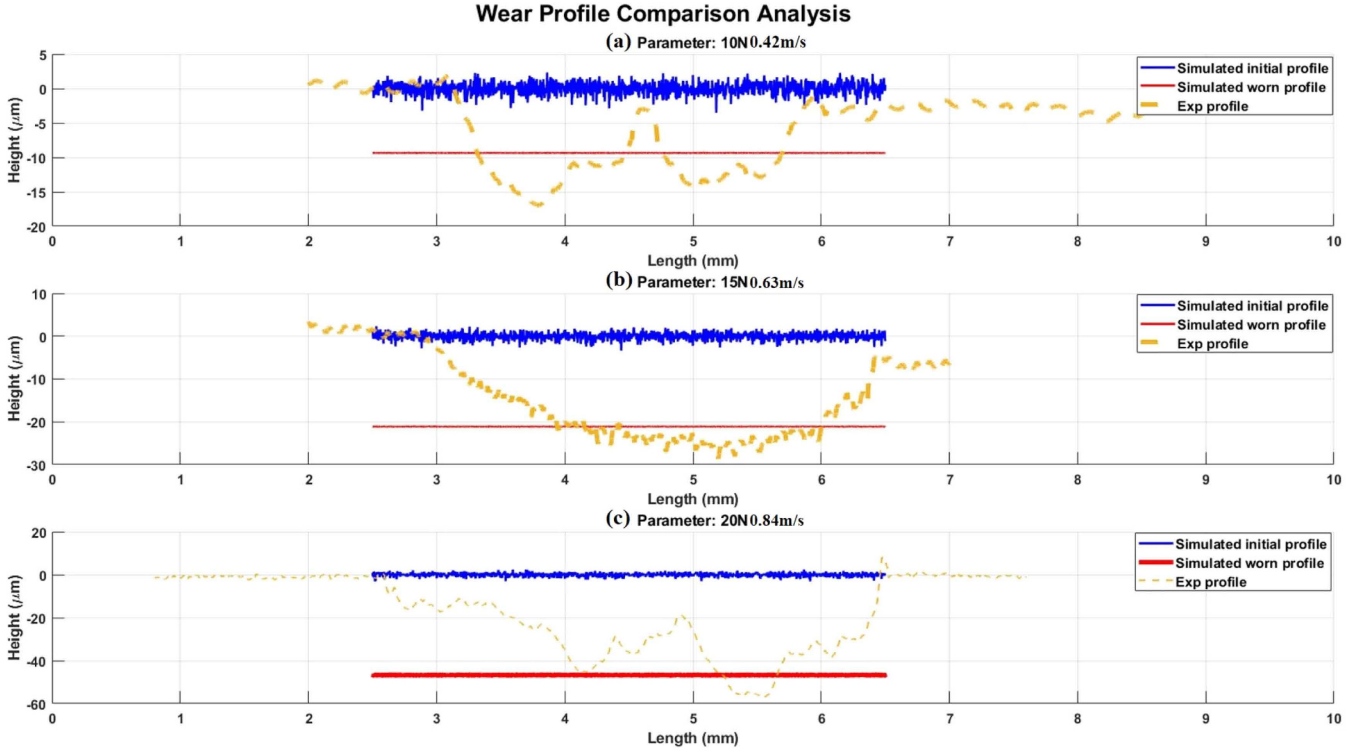


Fig. 9. Wear profile comparison between simulation and experiment under different load–speed conditions. The simulated initial surface profile, simulated worn profile, and experimentally measured wear profile are plotted as height (μm) versus track length (mm) for: (a) 10 N, 0.42 m/s; (b) 15 N, 0.63 m/s; and (c) 20 N, 0.84 m/s.

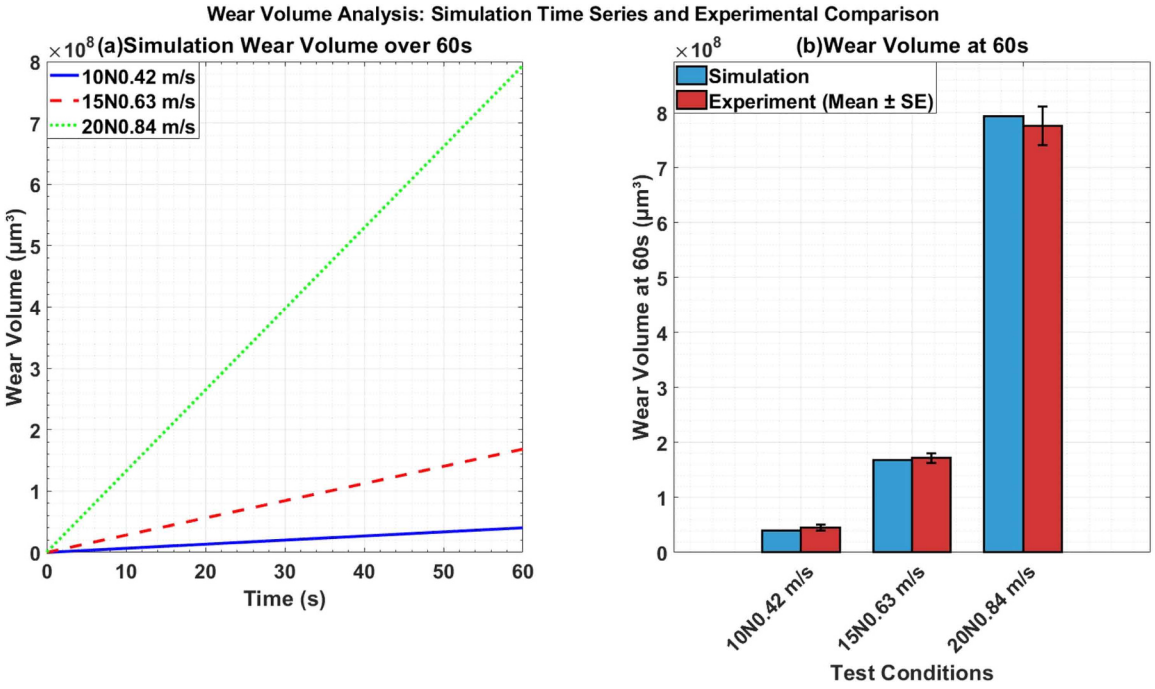


Fig. 10. Wear volume evolution and experimental validation under different load–speed conditions. (a) Simulated wear volume over 60 s for 10 N–0.42 m/s, 15 N–0.63 m/s, and 20 N–0.84 m/s. (b) Wear volume at 60 s: simulation vs. experiment (mean ± SE).

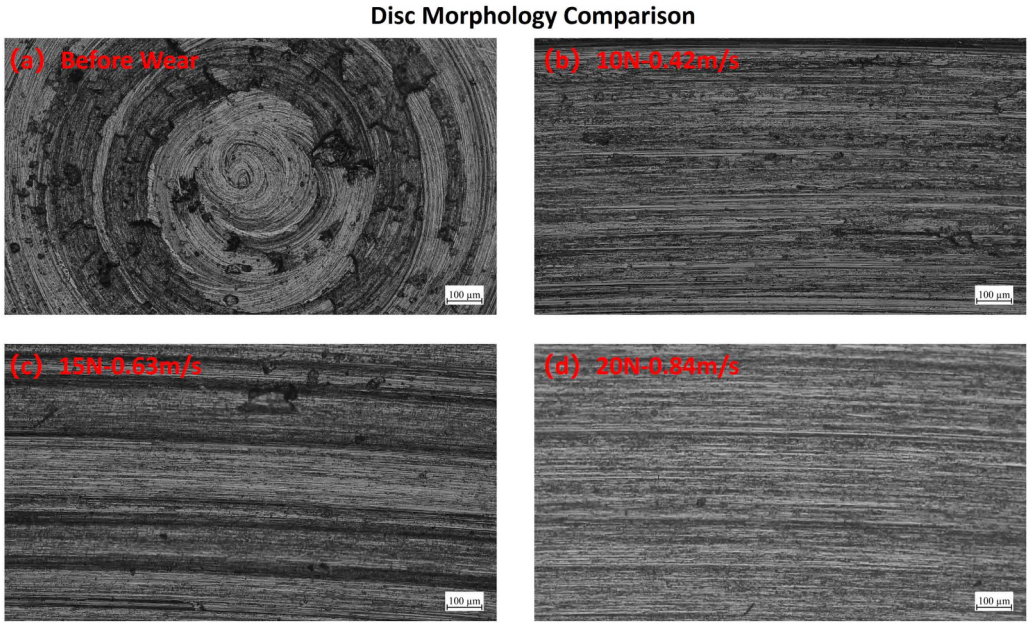


Fig. 11. Disc surface morphology before and after wear under different loading conditions, (a) Before wear, (b) 10 N–0.42 m/s, (c) 15 N–0.63 m/s, and (d) 20 N–0.84 m/s.

predictive capability beyond the data used for parameter identification.

The left plot depicts the simulated wear volume over 60 s, demonstrating a clear linear increase in wear. The 20 N at 0.84 m/s condition exhibits a steep linear increase, reaching approximately $8 \times 10^8 \mu m^3$, followed by the 15 N at 0.63 m/s and 10 N at 0.42 m/s conditions, with the latter showing the least wear. The right plot compares the simulated and experimentally measured wear volumes at 60 s. The simulation accurately captures the trend and magnitude of wear volume growth, thereby validating the model's predictive capability.

3.4. Microscopic characterization of wear scars and EDS analysis

To investigate the underlying wear mechanisms, the morphology of the disc was observed via optical microscopy, and the EDS Analysis were performed on the pin samples. The Fig. 11, illustrating the micro-morphological changes of a disc sample before and after wear tests under varying loads and sliding speeds, with a consistent 100 μm scale. Fig. 11 (a) shows the pristine "Before Wear" surface with a spiral-patterned texture, while Fig. 11 (b) through (d) depict progressive wear: shows dense and deep grooves with a pit along the sliding

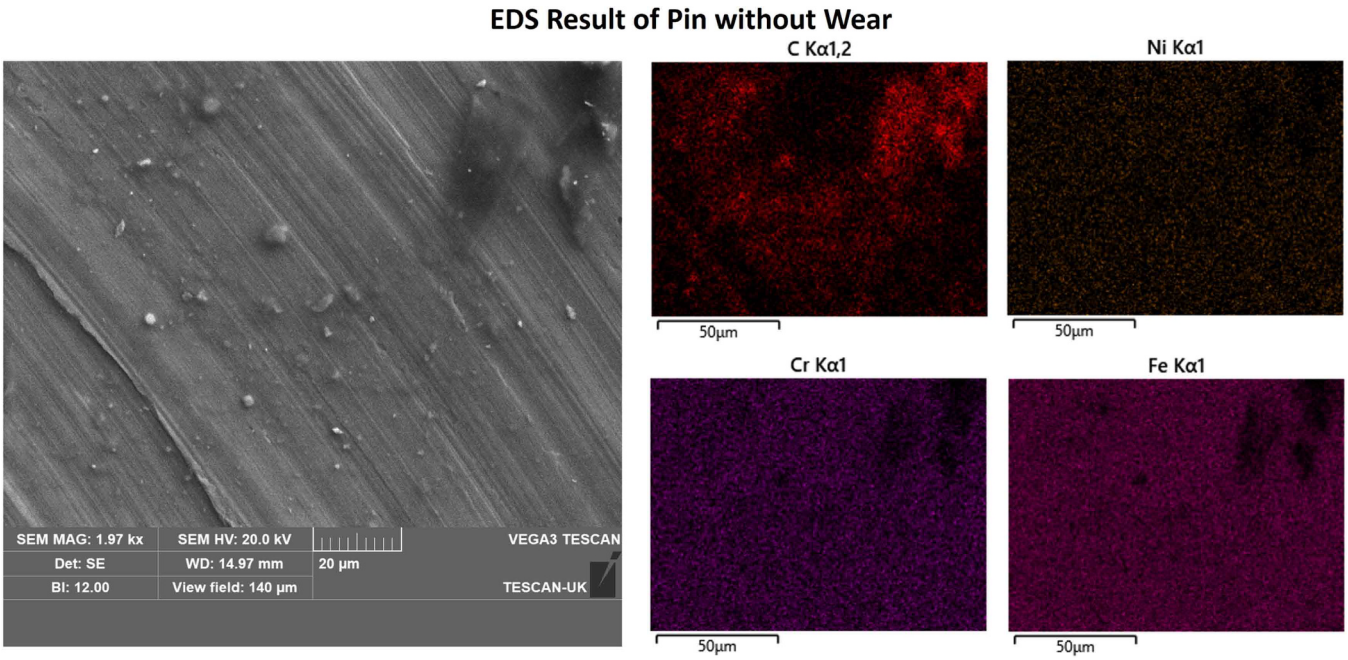


Fig. 12. Micromorphology and element distribution of pin without wear.

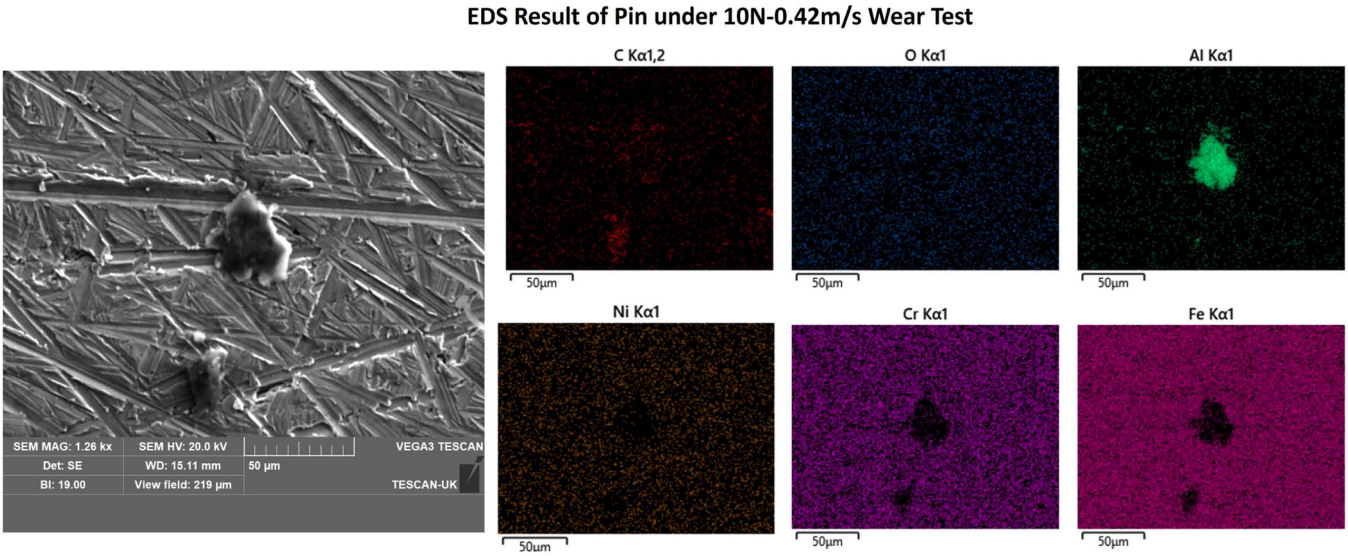


Fig. 13. Micromorphology and element distribution of pin under 10N0.42 m/s wear test.

direction on surfaces, which indicating severe abrasive wear occurred on disc surfaces.

Fig. 12 presents the composite analysis of the pin sample prior to wear, detailing the distribution of carbon, nickel, chromium, and iron, which align with the typical composition of 304 stainless steel. The leftmost panel features the SEM micrograph of the unworn pin surface, revealing a textured appearance with parallel grooves and scattered small particles or debris, characteristic of its as-manufactured condition.

Fig. 13, Fig. 14, and Fig. 15 show a progression of surface damage under different experimental conditions: at 10N-0.42 m/s, the surface features a wear scratches with a prominent dark debris cluster; at 15N-0.63 m/s, the damage intensifies with more widespread debris and roughening; and at 20N-0.84 m/s, the surface exhibits severe abrasion with extensive material loss and larger debris accumulations.

The EDS maps reveal increasing oxygen concentrations (indicating oxidation) and localized aluminum presence (from aluminium wear debris trapped at contact region being pressed into the pin or the adhesive wear occurs between the pin and the disc) as the load and speed increase, with carbon, iron, nickel, and chromium distributions remaining relatively uniform but showing localized enrichment around debris sites.

Compared to the previous "EDS Result of Pin without Wear" (Fig. 12), which displayed a uniform elemental distribution and a textured but undamaged surface with parallel grooves, the wear-tested samples show significant morphological degradation and new elemental signatures (e.g., oxygen and aluminum), reflecting oxidative wear and material transfer under increasing tribological stress.

In the experiments conducted, adhesive wear emerged as the primary wear mechanism. Given that the Archard model is best suited for light to medium loads, stable conditions, and metal contacts dominated by adhesive wear [52,53], it represents a logical choice for simulating the wear process.

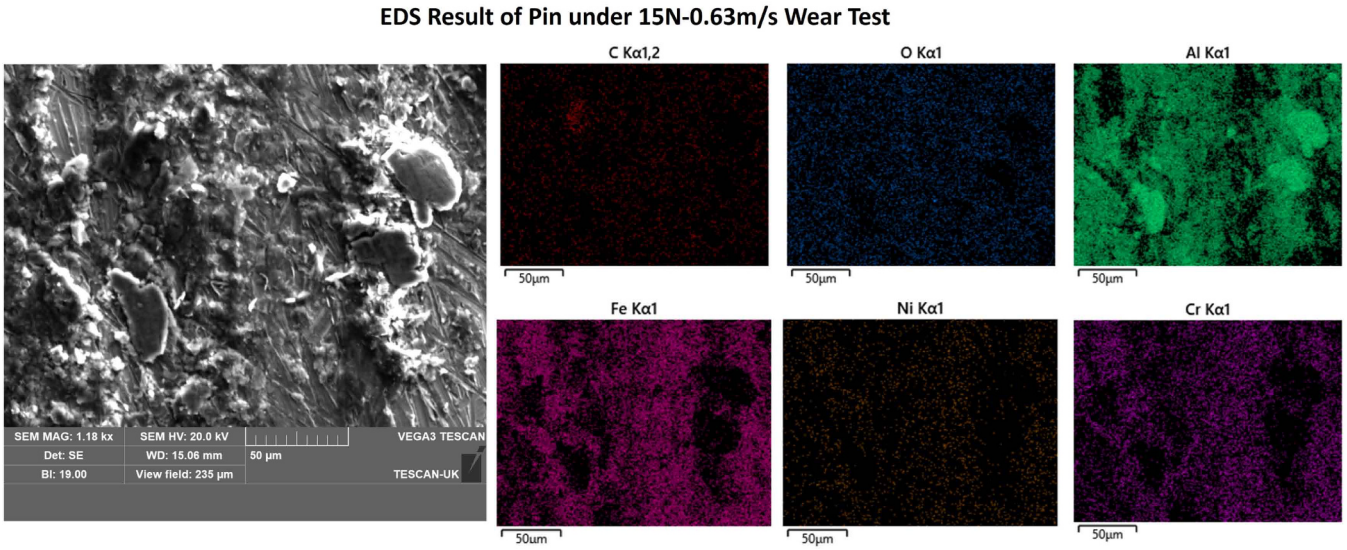


Fig. 14. Micromorphology and element distribution of pin under 15N0.63 m/s wear test.

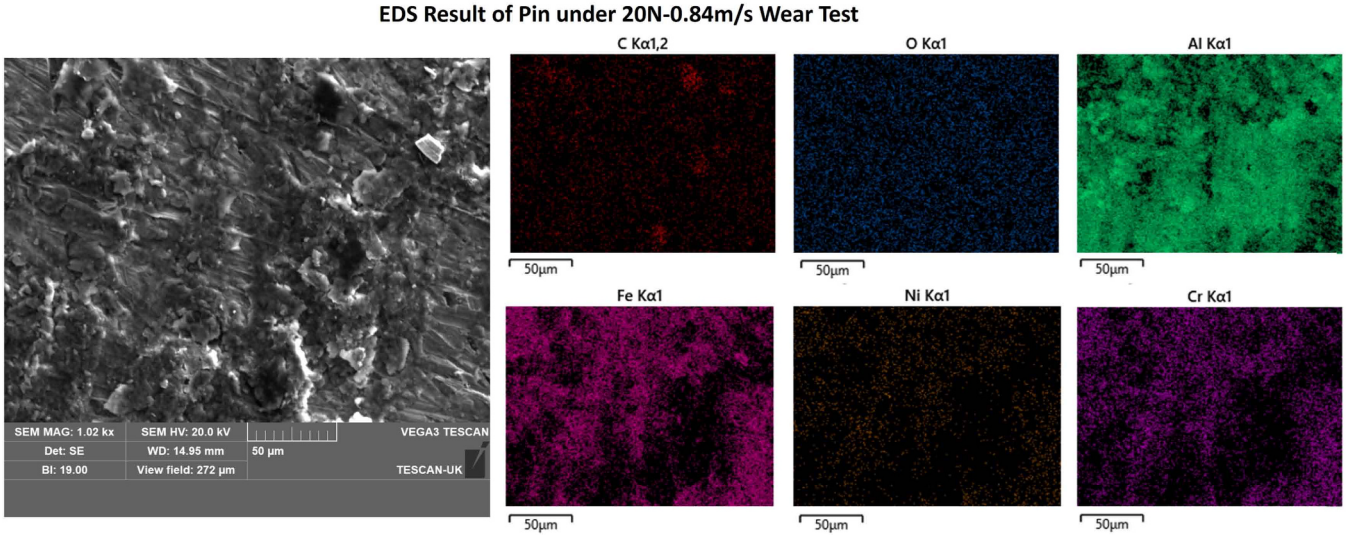


Fig. 15. Micromorphology and element distribution of pin under 20N0.84 m/s wear test.

3.5. Noise prediction

Fig. 16 presents a comparative analysis of cumulative noise generation over time under three different test conditions: 10 N at 0.42 m/s, 15 N at 0.63 m/s, and 20 N at 0.84 m/s. Each subplot shows the mean cumulative noise from five repeated tests, with shaded regions indicating the standard error (SE). Across all three conditions, cumulative noise increases over time and follows a nonlinear trend, gradually levelling off toward the end of the 60-second test duration. The magnitude of cumulative noise is positively correlated with load and sliding speed: the 10 N condition peaks at around 0.10 Pa, the 15 N condition reaches approximately 0.19 Pa, and the 20 N condition climbs to nearly 0.40 Pa. These results indicate that both mechanical load and sliding velocity significantly amplify noise generation. Higher sliding speeds enhance the number of collisions between asperities per unit time, which is considered a factor that can amplify the noise [13,54]. Higher loads promote the formation of wear debris. In this process, the stored elastic strain energy is released as acoustic energy [55,56].

The experiments under each configuration were replicated five times. For each configuration, one dataset was randomly selected to fit the parameter A in Eq. (7), and subsequently integrated with the wear volume and COF from the numerical simulation to predict the noise. The predicted noise from the current model was then compared with the remaining four experimental datasets and Lontin's model [13] for validation, as shown in Fig. 17.

Each subplot displays the time evolution of noise pressure (left y-axis, in Pa) from 0 to 60 s, alongside relative errors (right y-axis, in %). The experimental noise band (blue shaded area) exhibits an initial low pressure that decays over time, with peak values increasing with load: approximately 0.15 Pa at 10 N, 0.25 Pa at 15 N, and 0.5 Pa at 20 N, reflecting amplified noise generation due to elevated friction or energy dissipation. The Current Model closely aligns with the experimental data, yielding average relative errors of 13.83 % (10 N), 16.09 % (15 N), and 14.40 % (20 N), while the Lotin Model consistently overpredicts, resulting in higher errors of around 29 % across all conditions. Relative errors start elevated (40–100 %) during early transients and decrease to below 20 % by 30–40 s, with the Current Model demonstrating superior accuracy. The fitted parameter A decreases with increasing load (2.49×10^{-4} kg·m^{-1}·s^{-2} at 10 N, 2.25×10^{-4} at 15 N, and 1.92×10^{-4}at 20 N), suggesting an inverse relationship possibly

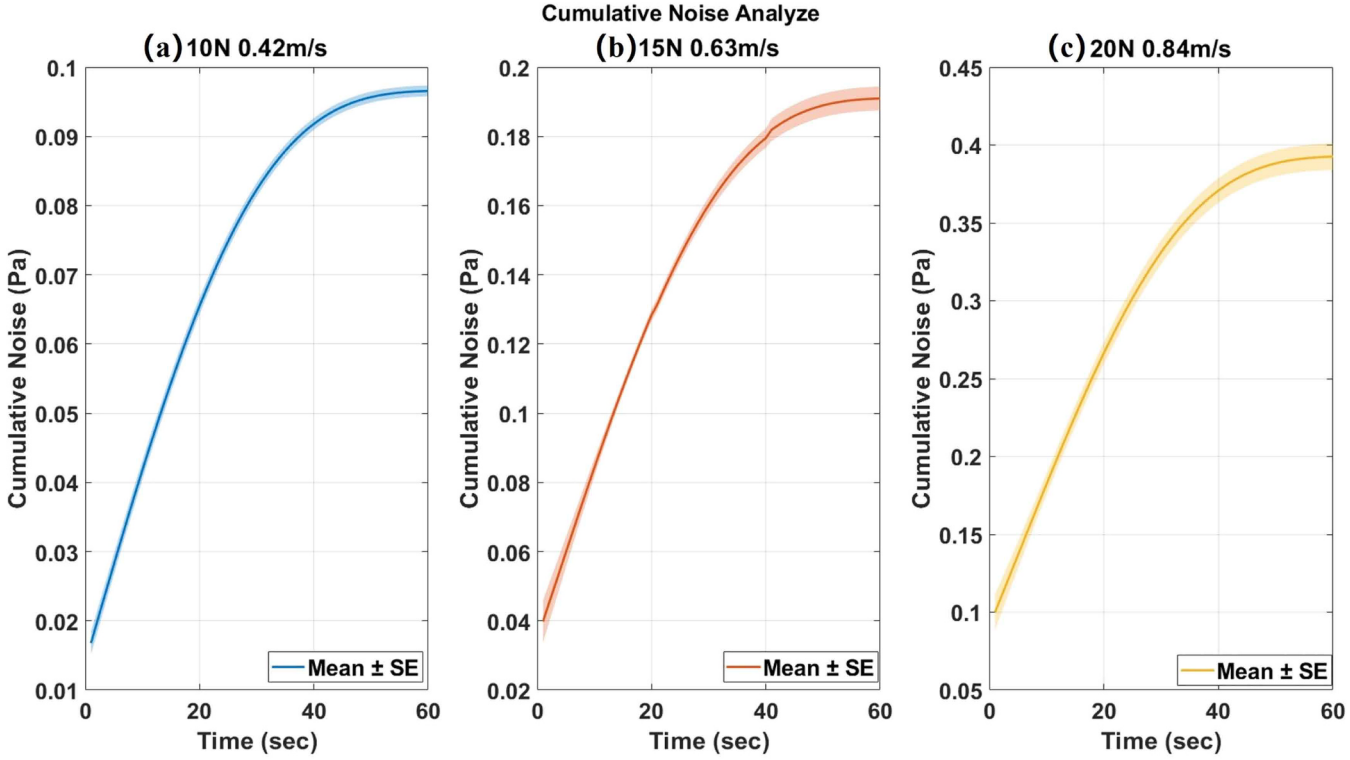


Fig. 16. Cumulative noise evolution under varying load and speed conditions, (a) 10 N–0.42 m/s, (b) 15 N–0.63 m/s, and (c) 20 N–0.84 m/s.

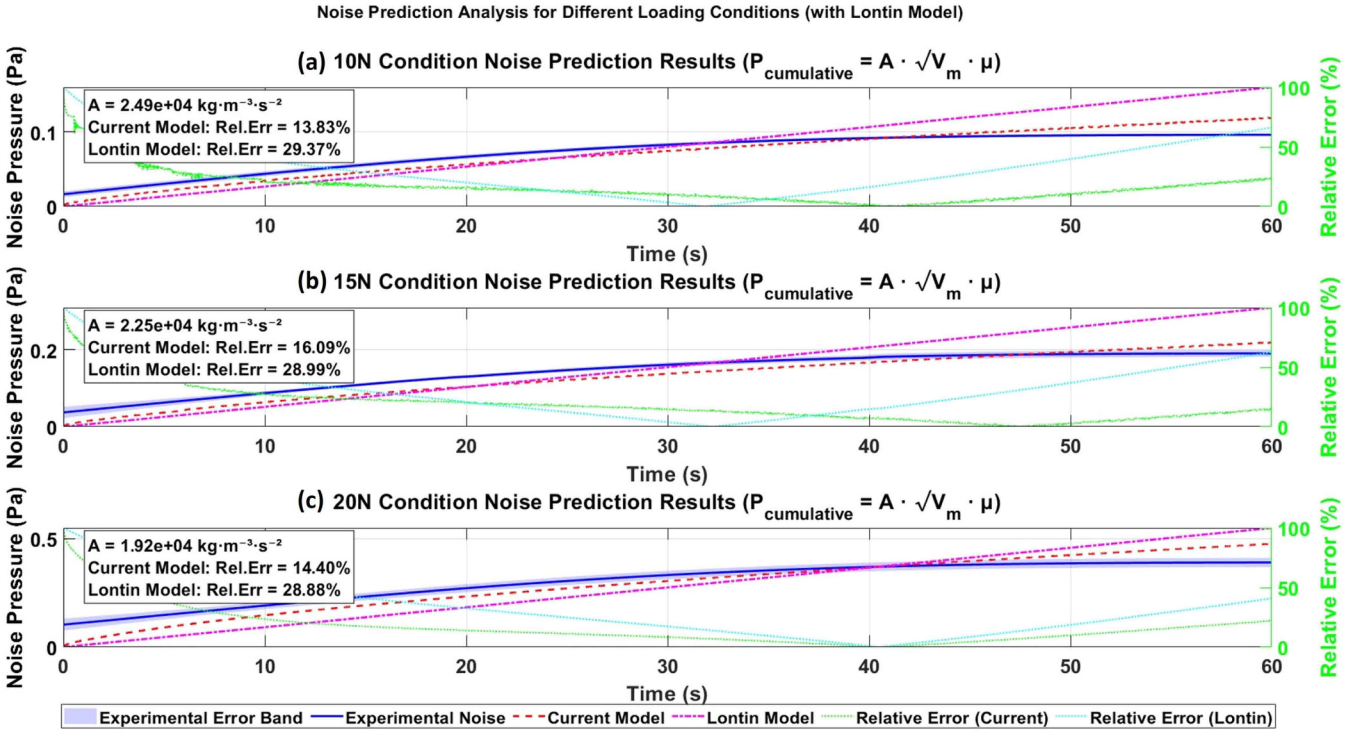


Fig. 17. Noise prediction comparison under different loading conditions, (a) 10 N–0.42 m/s, (b) 15 N–0.63 m/s, and (c) 20 N–0.84 m/s.

linked to load-dependent damping or material properties. Overall, the Current Model outperforms the Lontin Model in capturing transient dynamics and load effects, supporting its efficacy for noise prediction in loaded systems.

4. Conclusion

This study presents a comprehensive multi-physics numerical framework that integrates advanced contact mechanics, scale-dependent adhesion friction, asperity interlocking effects, Archard-

based wear evolution, and symbolic regression-derived noise prediction to simulate the tribological behaviour of an aluminium disc against a stainless-steel pin under varying load and sliding speed conditions.

The simulation demonstrates strong predictive capability, accurately capturing the temporal evolution of the coefficient of friction (COF), with steady-state values between 0.6 and 0.8 that increase with loading severity, reflecting the transition from adhesion-dominated to interlocking-dominated friction mechanisms.

Contact analysis reveals load-dependent stabilization of real contact area and asperity counts, while wear profiles and volumes show linear accumulation trends that align well with experimental measurements, though slight underestimations in maximum wear depth highlight the influence of unmodeled factors such as thermal softening and debris effects.

Noise predictions, based on cumulative sound pressure linked to wear volume and COF, achieve mean relative errors of 13–16 % across conditions, underscoring the model's utility in forecasting acoustic emissions from tribological interactions.

The proposed methodology advances the understanding of surface evolution in sliding contacts by distinguishing between adhesive and mechanical friction contributions, enabling dynamic topography updates, and linking these with noise generation. This offers a potential tool for non-invasive inspection of frictional pairs in engineering applications where friction, wear, and noise are critical performance metrics.

While the framework effectively bridges microscopic asperity behaviour with macroscopic observables, limitations arise from simplifications in interlocking friction modelling and the exclusion of environmental variables. Future research could incorporate thermal-mechanical coupling, debris dynamics, and environmental factors to further enhance predictive accuracy and extend applicability to diverse tribosystems.

Statement of originality

1) This manuscript is an original work, previously unpublished, not currently under review by another journal, and will not be republished in its current form—in English or any other language—without explicit written permission from the publisher following acceptance.
2) The content of this manuscript does not include any previously published material by the authors or others, except where properly cited in the text.

CRediT authorship contribution statement

Yang Tian: Writing – original draft, Software, Methodology, Investigation, Formal analysis, Data curation, Conceptualization. **Muhammad Khan:** Supervision, Methodology, Conceptualization.

Declaration of Generative AI and AI-assisted technologies in the writing process

During the preparation of this work the author(s) used Grok 3 to improve the language and readability of the paper. After using this tool/service, the author(s) reviewed and edited the content as needed and take(s) full responsibility for the content of the publication.

Declaration of Competing Interest

The authors affirm that they are not aware of any competing financial interests or personal relationships that could have impacted the research presented in this manuscript.

Data availability

Data will be made available on request.

References

[1] Lontin K, Khan M. Interdependence of friction, wear, and noise: a review. Friction 2021;9:1319–45. https://doi.org/10.1007/s40544-021-0500-x.
[2] Tian Y, Khan M, Yuan H, Zheng B. Wear modeling and friction-induced noise: a review. Friction 2025. https://doi.org/10.26599/FRICT.2025.9441124.
[3] Holmberg K, Erdemir A. Influence of tribology on global energy consumption, costs and emissions. Friction 2017;5:263–84. https://doi.org/10.1007/s40544-017-0183-5.
[4] Heo J, Lee J, Kim S, Alfantazi A, Cho SO. Corrosion resistance of austenitic stainless steel using cathodic plasma electrolytic oxidation. Surf Coat Technol 2023;462. https://doi.org/10.1016/j.surfcoat.2023.129448.
[5] Hirsch J, Al-Samman T. Superior light metals by texture engineering: optimized aluminum and magnesium alloys for automotive applications. Acta Mater 2013;61:818–43. https://doi.org/10.1016/j.actamat.2012.10.044.
[6] Mert F. Dry sliding wear behaviour of as-cast AZ31B magnesium alloy. Mechanika 2017;23:728–34. https://doi.org/10.5755/j01.mech.23.5.15761.
[7] Kapsa P. Tribology at Different Scales. Adv Eng Mater 2001;3:531. https://doi.org/https://advanced.onlinelibrary.wiley.com/doi/10.1002/1527-2648(200108)3:8%3C531::AID-ADEM531%3E3.0.CO;2-1.
[8] De Moerlooze K, Al-Bender F, Van Brussel H. A generalised asperity-based friction model. Tribol Lett 2010;40:113–30. https://doi.org/10.1007/s11249-010-9645-x.
[9] Czichos H. Tribology and its many facets: from macroscopic to microscopic and nano-scale phenomena. Meccanica 2001;36:605–15. https://doi.org/10.1023/A:1016388517893.
[10] Le Bot A, Bou Chakra E. Measurement of friction noise versus contact area of rough surfaces weakly loaded. Tribol Lett 2010;37:273–81. https://doi.org/10.1007/s11249-009-9521-8.
[11] Ben Abdelounis H, Le Bot A, Perret-Liaudet J, Zahouani H. An experimental study on roughness noise of dry rough flat surfaces. Wear 2010;268:335–45. https://doi.org/10.1016/j.wear.2009.08.024.
[12] Ben Abdelounis H, Zahouani H, Le Bot A, Perret-Liaudet J, Tkaya MBen. Numerical simulation of friction noise. Wear 2011;271:621–4. https://doi.org/10.1016/j.wear.2010.07.014.
[13] Lontin K, Khan MA. Wear and airborne noise interdependency at asperitical level: Analytical modelling and experimental validation. Materials 2021;14. https://doi.org/10.3390/ma14237308.
[14] Lontin K, Khan M, Alharbi B. Investigation of the Effect of Temperature on the Wear Rate and Airborne Noise in Sliding Wear. Materials 2022;15. https://doi.org/10.3390/ma15030812.
[15] Basit K, Shams H, Khan MA, Mansoor A. Vibration Analysis Approach to Model Incremental Wear and Associated Sound in Multi-Contact Sliding Friction Mechanisms. J Tribol 2023;145. https://doi.org/10.1115/1.4062720.
[16] Khan MA, Basit K, Khan SZ, Khan KA, Starr AG. Experimental assessment of multiple contact wear using airborne noise under dry and lubricated conditions. Proc Inst Mech Eng Part J J Eng Tribology 2017;231:1503–16. https://doi.org/10.1177/1350650117700341.
[17] Tian Y, Zheng B, Khan M, Yang Y. Real-time prediction of wear morphology and coefficient of friction using acoustic signals and deep neural networks in a tribological system. Processes 2025;13. https://doi.org/10.3390/pr13061762.
[18] Tian Y, Khan M, Deng H, Omar I. Quantifying the interrelationship between friction, wear, and noise: a comparative study on aluminum, brass, and steel. Tribol Int 2025;203. https://doi.org/10.1016/j.triboint.2024.110403.
[19] Tian Y, Zheng B, Khan M, He F. Influence of sliding direction relative to layer orientation on tribological performance, noise, and stability in 3D-printed ABS components. Tribol Int 2025;210. https://doi.org/10.1016/j.triboint.2025.110762.
[20] Kang M, Deng Y, Du F, Liu S, Wang B, Zhao MC. Hot deformation constitutive modeling of 6111 aluminum alloy linking Z-parameter to the associated microstructural evolution and precipitation strengthening. J Mater Res Technol 2025;39:8562–76. https://doi.org/10.1016/j.jmrt.2025.11.141.
[21] Han M, Wu Y, Zong X, Shen Y, Zhang F, Lou H, et al. Lightweight single-phase Al-based complex concentrated alloy with high specific strength. Nat Commun 2024;15. https://doi.org/10.1038/s41467-024-51387-6.
[22] Tian Y, Khan M, Deng H, Omar I. Quantifying the interrelationship between friction, wear, and noise: a comparative study on aluminum, brass, and steel. Tribol Int 2025;203. https://doi.org/10.1016/j.triboint.2024.110403.
[23] Pogačnik A, Kalin M. How to determine the number of asperity peaks, their radii and their heights for engineering surfaces: a critical appraisal. Wear 2013;300:143–54. https://doi.org/10.1016/j.wear.2013.01.105.
[24] Ghatrehsamani S, Akbarzadeh S, Khonsari MM. Experimentally verified prediction of friction coefficient and wear rate during running-in dry contact. Tribol Int 2022;170. https://doi.org/10.1016/j.triboint.2022.107508.
[25] Kucharski S, Starzynski G. Study of contact of rough surfaces: modeling and experiment. Wear 2014;311:167–79. https://doi.org/10.1016/j.wear.2014.01.009.
[26] Pugliese G, Tavares SMO, Ciulli E, Ferreira LA. Rough contacts between actual engineering surfaces. Part Ii Contact Mech Wear 2008;264:1116–28. https://doi.org/10.1016/j.wear.2007.08.027.

[27] Persson BNJ. Functional properties of rough surfaces from an analytical theory of mechanical contact. MRS Bull 2022;47:1211–9. https://doi.org/10.1557/s43577-022-00472-6.
[28] Hertz H. Ueber die Berührung fester elastischer Körper. Crll 1882;1882:156–71. https://doi.org/10.1515/crll.1882.92.156.
[29] Greenwood JA, Tripp JH. The elastic contact of rough spheres. J Appl Mech 1967; 34:153–9. https://doi.org/10.1115/1.3607616.
[30] Pullen J, Williamson JBP. On the plastic contact of rough surfaces. Proc R Soc Lond A Math Phys Sci 1972;327:159–73. https://doi.org/10.1098/rspa.1972.0038.
[31] Zhao Y, Maietta DM, Chang L. Asperity Micro Model Inc Transit Elastic Deform Full Plast Flow 2000.
[32] Gauthier C, Durier A-L, Fond C, Schirrer R. Mechanical Analysis of the Scratching Properties of Coated Polymers. Tribology and Interface Engineering Series, 51. Elsevier; 2006. p. 1–21. https://doi.org/10.1016/S0167-8922(06)80037-4.
[33] de Wit CC, Lischinsky P, Åström KJ, Olsson H. A New Model for Control of Systems with Friction. IEEE Trans Autom Contr 1995;40:419–25. https://doi.org/10.1109/9.376053.
[34] Liao D, Shao W, Tang J, Li J. An improved rough surface modeling method based on linear transformation technique. Tribol Int 2018;119:786–94. https://doi.org/10.1016/j.triboint.2017.12.008.
[35] Hurtado JA, Kim K. Scale effects in friction of single–asperity contacts. I. From concurrent slip to single–dislocation–assisted slip. Proc R Soc Lond Ser A Math Phys Eng Sci 1999;455:3363–84. https://doi.org/10.1098/rspa.1999.0455.
[36] Hurtado JA, Kim K. Scale effects in friction of single–asperity contacts. I. From concurrent slip to single–dislocation–assisted slip. Proc R Soc Lond Ser A Math Phys Eng Sci 1999;455:3363–84. https://doi.org/10.1098/rspa.1999.0455.
[37] Archard JF. The wear of metals under unlubricated conditions. Proc R Soc Lond A Math Phys Sci 1956;236:397–410. https://doi.org/10.1098/rspa.1956.0144.
[38] Archard JF. Contact and rubbing of flat surfaces. J Appl Phys 1953;24:981–8. https://doi.org/10.1063/1.1721448.
[39] Ghosh A, Sadeghi F. A novel approach to model effects of surface roughness parameters on wear. Wear 2015;338–339:73–94. https://doi.org/10.1016/j.wear.2015.04.022.
[40] Beheshti A, Khonsari MM. A thermodynamic approach for prediction of wear coefficient under unlubricated sliding condition. Tribol Lett 2010;38:347–54. https://doi.org/10.1007/s11249-010-9614-4.
[41] Beheshti A, Khonsari MM. An engineering approach for the prediction of wear in mixed lubricated contacts. Wear 2013;308:121–31. https://doi.org/10.1016/j.wear.2013.10.004.
[42] Aghababaei R, Warner DH, Molinari J-F. Critical length scale controls adhesive wear mechanisms. Nat Commun 2016;7:11816. https://doi.org/10.1038/ncomms11816.
[43] Brink T, Frérot L, Molinari J-F. A parameter-free mechanistic model of the adhesive wear process of rough surfaces in sliding contact. J Mech Phys Solids 2021;147: 104238. https://doi.org/10.1016/j.jmps.2020.104238.
[44] Frérot L, Aghababaei R, Molinari JF. A mechanistic understanding of the wear coefficient: From single to multiple asperities contact. J Mech Phys Solids 2018; 114:172–84. https://doi.org/10.1016/j.jmps.2018.02.015.
[45] Gloag R, Ding G, Christie JR, Buchmann G, Beekman M, Oldroyd BP. An invasive social insect overcomes genetic load at the sex locus. Nat Ecol Evol 2016;1. https://doi.org/10.1038/s41559-016-0011.
[46] Saito S, Ochiai T, Yoshizawa F, Dao M. Rolling behavior of a micro-cylinder in adhesional contact. Sci Rep 2016;6. https://doi.org/10.1038/srep34063.
[47] Mohd Yusof NF, Mohd Ripin Z. Experimental and finite element analysis of surface asperity geometry during the running-in phase of rolling contact. Proc Inst Mech Eng C J Mech Eng Sci 2024;238:9698–710. https://doi.org/10.1177/09544062241263412.
[48] Verma J, Nagdeve L, Kumar H. Tribological investigations into pin-on-disc tribometer under dry sliding conditions at various temperature ranges. Proc Inst Mech Eng Part E J Process Mech Eng 2022;236:178–86. https://doi.org/10.1177/09544089211042954.
[49] Ciulli E, Bassani R. Influence of vibrations and noise on experimental results of lubricated non-conformal contacts. Proc Inst Mech Eng Part J Eng Tribology 2006; 220:319–31. https://doi.org/10.1243/13506501JET138.
[50] Schaffelhofer S, Sartori M, Scherberger H, Farina D. Musculoskeletal representation of a large repertoire of hand grasping actions in primates. IEEE Trans Neural Syst Rehabil Eng 2015;23:210–20. https://doi.org/10.1109/TNSRE.2014.2364776.
[51] Wang G, Zhang Y, Liao G, Zhang X, Hu Z, Wang W. Experimental study on the interface topography evolution and vibration monitoring in thrust ball bearings induced by particulate contamination. J Adv Mech Des Syst Manuf 2023;17. https://doi.org/10.1299/jamdsm.2023jamdsm0029.
[52] Delaney B, Wang QJ. Archard's law: foundations, extensions, and critiques. Encyclopedia 2025;5:124. https://doi.org/10.3390/encyclopedia5030124.
[53] Delaney BC, Wang QJ, Aggarwal V, Chen W, Evans RD. A contemporary review and data-driven evaluation of archard-type wear laws. Appl Mech Rev 2025;77. https://doi.org/10.1115/1.4068297.
[54] Ben Abdelounis H, Zahouani H, Le Bot A, Perret-Liaudet J, Tkaya MBen. Numerical simulation of friction noise. Wear 2011;271:621–4. https://doi.org/10.1016/j.wear.2010.07.014.
[55] Zmitrowicz A. 2005. WEAR DEBRIS: A REVIEW OF PROPERTIES AND CONSTITUTIVE MODELS. vol. 43.
[56] Kovanen R, Laiholahti OP, Juoksukangas J, Vippola M, Hintikka J, Mäntylä A, et al. Acoustic emissions caused by fretting induced adhesion, wear and cracking. Tribol Finn J Tribology 2024;41:52–3. https://doi.org/10.30678/fjt.154999.



https://dspace.org/

Experimentally validated numerical model for multi-physics simulation of friction, wear, and noise in dry sliding pin-on-disc configurations

Tian, Yang; Khan, Muhammad A.

2026-07
Elsevier
https://doi.org/10.1016/j.triboint.2026.111855
Tian Y, Khan M. (2026) Experimentally validated numerical model for multi-physics simulation of friction, wear, and noise in dry sliding pin-on-disc configurations. Tribology International, Volume 219, July 2026, Article number 111855

Downloaded from a DSpace repository. https://dspace.org/